nature sustainability

ARTICLES

https://doi.org/10.1038/s41893-020-0586-6

Check for updates

Sustainable lead management in halide perovskite solar cells

So Yeon Park[1,2,9], Ji-Sang Park[3,9], Byeong Jo Kim[1,4], Hyemin Lee[5], Aron Walsh[6,7], Kai Zhu[8], Dong Hoe Kim[5]✉ and Hyun Suk Jung[1]✉

Despite the rapid development of perovskite solar cells (PSCs) toward commercialization, the toxic lead (Pb) ions in PSCs pose a potential threat to the environment, health and safety. Managing Pb via recycling represents a promising approach to mitigating its toxicity. However, managing Pb from commonly used organic solvents has been challenging due to the lack of suitable Pb adsorbents. Here, we report a new adsorbent for both separation and recovery of Pb from PSC pollutants. The synthesized iron-incorporated hydroxyapatite possesses a strongly negatively charged surface that improves electrostatic interaction through surface-charge delocalization, thus leading to enhanced Pb adsorption. We demonstrate the feasibility of a complete Pb management process, including the purification of Pb-containing non-aqueous solvents below 15 parts per 10^9, a level compliant with the standards of the US Environmental Protection Agency, as well as recycling of 99.97% of Pb ions by forming lead iodide.

Lead (Pb) halide perovskite, containing organic or inorganic cations, lead ions and halide ions in the perovskite structure, shows superior photovoltaic performance and stability, as well as immense potential for being scaled up, which makes it the most promising emerging photovoltaic technology[1–6]. However, potentially long-term risks may be incurred due to treatment of Pb-containing non-aqueous waste during fabrication as well as the continuous exposure to Pb from waste or the device itself. Therefore, the environmental, health and safety effects of the materials and processes involved could be a major concern in perovskite solar cell (PSC) commercialization[7–11]. The photovoltaic industry has an existing exemption to the Restriction of Hazardous Substances Directive—namely, cadmium telluride (CdTe) solar cells. These cells have been commercialized despite the hazardous element Cd because Cd is controlled through a meticulous management and recycling programme—from production to disposal of the CdTe[7,10]. To follow in CdTe's path, Pb halide PSCs must track and recycle Pb during all phases of a module's lifetime.

Several approaches have been considered for managing Pb from an aqueous solution, such as precipitation[12], membrane filtration[13] and adsorption using adsorbent[14,15] but none has been established yet for the non-aqueous pollutant. We want to recover a Pb-containing non-aqueous liquid pollutant, generated while fabricating PSCs, in an industrial application at below-ppm levels and do so cost effectively. The adsorption approach is one of the best candidates because it can enhance the reactivity with Pb, making it easy to retrieve from the solution after adsorption, and it can be scaled up for commercialization[15].

Various strategies exist to improve adsorption capability of adsorbents, which could adsorb atoms, ions or molecules from gas, liquid or salt-dissolved solution on their surface, such as increased surface area, chemical activation of the absorption surface and formation of a hybrid composite. Of these, hybrid composites have been explored most widely because they efficiently incorporate all the advantages mentioned[15–19]. However, hybrid composites have a major disadvantage—the trade-off between functionality and decreasing the density of active surface sites due to unequal absorption properties of each material.

A strategy to address this trade-off is to strengthen the negative surface and enhance the electrostatic interaction via charge delocalization using doping by metallic elements (for example, iron (Fe) and magnesium (Mg)) on the active surface sites in hybrid composites. Among various negatively charged Pb adsorbents, such as manganese dioxide (MnO_2), zeolites, or hydroxyapatite ($Ca_{10}(PO_4)_6(OH)_2$, HAP)[14,15,20,21] has many advantages over its competitors. HAP is inexpensive and is bio- and environment friendly, and it has Earth-abundant components and easily controllable morphology and size. But in particular, it has lattice-expansion flexibility for a broad range of doping, and it has a malleable surface charge via doping[20–23]. These two properties are especially important because they can readily control the surface charge of HAP crystals via the various choices of dopants.

In this paper, we report on sustainable Pb management, during the entire fabrication of PSCs, via the design of an Fe-decorated HAP (HAP/Fe) hollow composite. HAP/Fe serves two critical functions: (1) it modifies the surface charge to enhance Pb adsorption capacity, and (2) it assigns magnetism for easy collection of Pb-adsorbed HAP/Fe from solvents. The purified polar solvent dropped below 15 parts per 10^9 (ppb) of Pb, meeting the standards of the US Environmental Protection Agency (EPA). Using the solubility difference between HAP/Fe and Pb^{2+} ions under different pH

[1]School of Advanced Materials Science and Engineering, Sungkyunkwan University, Suwon, Republic of Korea. [2]Nanomechanical Systems Research Division, Korea Institute of Machinery and Materials, Daejeon, Republic of Korea. [3]Department of Physics, Kyungpook National University, Daegu, Republic of Korea. [4]Department of Chemistry—Ångström Laboratory, Physical Chemistry, Uppsala University, Uppsala, Sweden. [5]Department of Nanotechnology and Advanced Materials Engineering, Sejong University, Seoul, Republic of Korea. [6]Thomas Young Centre and Department of Materials, Imperial College London, London, UK. [7]Department of Materials Science and Engineering, Yonsei University, Seoul, Republic of Korea. [8]Chemistry and Nanoscience Center, National Renewable Energy Laboratory, Golden, CO, USA. [9]These authors contributed equally: So Yeon Park, Ji-Sang Park. ✉e-mail: donghoe.k@sejong.ac.kr; hsjung1@skku.edu

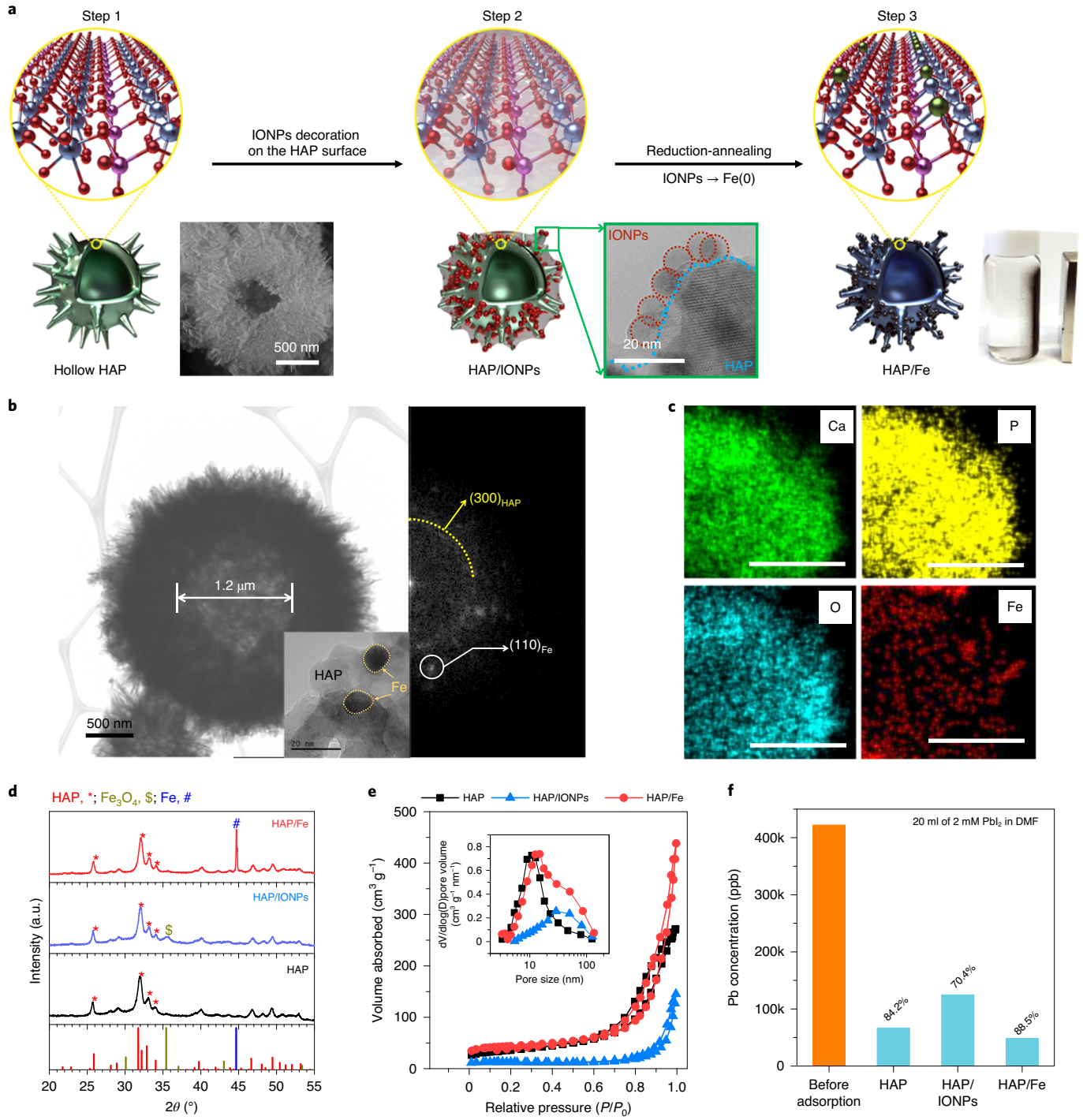

Fig. 1 | Synthesis of magnetic hollow HAP/Fe composite and its properties for Pb absorption. a, Schematic and representative images of the preparation steps of magnetic hollow HAP/Fe composites. First, hollow HAP was synthesized using the Kirkendall effect assisted anion-exchange process. The SEM image on the right is a broken hollow HAP particle. The next step is the attachment of IONPs to the surface of HAPs via hydrogen bonding to provide magnetic activity. The TEM image shows an IONP-decorated HAP surface. To form magnetic Fe on HAPs and remove surfactants, HAP/IONPs are annealed at 500 °C for 2 h under reductive 5 v/v% H_2/N_2 atmosphere. The synthesized HAP/Fe composite can be attached to the Nd magnet, as shown in the photo. **b**, Typical TEM images of prepared HAP/Fe. The inset magnified TEM image shows a sub-10-nm Fe particle on the HAP surface, and the reduced fast Fourier transform patterns are obtained from the inset image. **c**, Energy-dispersive X-ray spectroscopy mapping of HAP/Fe. Scale bar, 500 nm. **d**, XRD patterns of HAP, HAP/IONPs and HAP/Fe. **e**, N_2 adsorption–desorption isotherm and pore size distributions (insets) of HAP, HAP/IONPs and HAP/Fe. **f**, Feasibility of uptake of Pb in PbI_2/DMF using HAP/Fe. The 50-mg HAP, HAP/IONPs and HAP/Fe are dispersed in 20 ml of 2 mM PbI_2–DMF solution, separately.

values, we recycled Pb wastes as lead iodide (PbI_2) with a high recycling yield of 99.97%. The demonstrated devices using only recycled components (for example, recycled TiO_2/fluorine-doped tin oxide (FTO) substrate and PbI_2) confirmed the feasibility of sustainable fabrication of PSCs by showing comparable performance to that of fresh devices.

Synthesis of HAP/Fe

HAP/Fe hollow composites were synthesized via a three-step process, as illustrated in Fig. 1a. First, three-dimensional branched HAP hollow-structured particles were synthesized via a Kirkendall effect ion-exchange method based on $CaCO_3$ spheres[24,25]. The hollow interior of HAP is observed in a field-emission scanning electron microscope (FE-SEM) image (the first step in Fig. 1a). More than 1 μm in size and hollow, its nanorod building blocks, which are grown along the *c* axis, are revealed in high-resolution transmission electron microscope (HR-TEM) images (Supplementary Fig. 1a,b). Further, the low-magnification FE-SEM image in Supplementary Fig. 1c shows its morphological homogeneity. Supplementary Fig. 2 and Supplementary Table 1 illustrate the ability of this synthesis to scale up to tens of grams and the cost-effectiveness of raw materials for HAP and Fe. To enable the magnetic property of the HAPs, (3-aminopropyl)triethoxysilane (APTES)-functionalized HAP bonded with ~10-nm-sized iron oxide nanoparticles (IONPs). The IONPs had a citric acid ligand via hydrogen bonding between the amino group of APTES in HAP and the carboxy group in the citric acid ligand of the IONPs. The HR-TEM image in the second step in Fig. 1a shows the IONP-decorated surface of a HAP nanorod building block. Subsequently, the HAP/IONPs composites are annealed at 500 °C for 2 h under a reductive atmosphere to (1) form HAP/Fe composites with ~9.5-nm-sized pure Fe nanoparticles (Supplementary Fig. 3) and (2) remove the existing polymer ligand for improved magnetic property and surface area. As shown in Supplementary Fig. 4, the magnetic intensity of HAP/Fe is larger than that of HAP/IONPs, and these data help to better understand the magnetic properties of HAP/Fe composites taken by using a permanent neodymium (Nd) magnet, shown in the third step in Fig. 1a. Low- and high-resolution TEM images (Fig. 1b and inset image of Fig. 1b) also show that Fe nanoparticles are bound to hollow HAP microspheres. The fast Fourier transform patterns of HAP/Fe, which correspond to the magnified inset image of Fig. 1b, show the (300) plane of HAP and (110) plane of Fe. Energy-dispersive X-ray spectroscopy elements-mapping images reveal that Fe nanoparticles uniformly decorate the entire HAP particle (Fig. 1c and Supplementary Fig. 5). The X-ray diffraction (XRD) analyses of HAP, HAP/IONPs and HAP/Fe in Fig. 1d also confirm the successful formation of Fe after reduction annealing, with the obtained powder showing a sharp Fe peak at 44.7° corresponding to the (110) plane of Fe metal in the XRD pattern of HAP/Fe. As shown in Supplementary Fig. 6, the XRD patterns of HAP/Fe composites had no noticeable phase change after long-term exposure to both air and *N*,*N*-dimethylformamide (DMF), indicating that the HAP/Fe composite is quite stable for use as the adsorbent.

The results of Brunauer–Emmett–Teller (BET) and Barrett–Joyner–Halenda (BJH) analyses in Fig. 1e and Table 1 show the surface properties of HAP, HAP/IONPs and HAP/Fe composites. The HAP/Fe composite has the highest BET surface area and BJH total pore volume, corresponding to 152.9 $m^2 g^{-1}$ and 0.514 $cm^3 g^{-1}$, respectively, which is larger than those of the control HAPs. This improving phenomenon of surface properties can be described by the process of attachment of the IONPs with bulky functional polymer ligands and selective removal of the polymer ligands. The inset in Fig. 1e displays a substantial change in pore distribution during the IONPs decoration of the HAP surface, which is the drastic decrease of small pores, while an increase in the number of large pores. This implies that the nano-sized pores (~10 nm) of HAPs act as effective reaction sites to ligands of IONPs, and simultaneously, their sizeable functional polymer groups form large pores. After removing ligands through reduction annealing, the nano-sized pores are almost recovered, indicating that the decorated Fe nanoparticles have a negligible effect on the surface area of their HAP host.

Figure 1f presents the Pb-adsorbing property of prepared HAP, HAP/IONPs and HAP/Fe composites through a comparison of the Pb concentrations of 2 mM PbI_2–DMF solution before and after filtration with 50 mg of particles. As expected, improvement in the Pb-adsorption property via control of the surface electrostatic property after Fe-decorating the HAP/Fe composite yielded the highest adsorbing property compared with those of others. We further performed a Pb adsorption test using HAP and HAP/Fe under varied conditions, such as the type of solvent, amount of adsorbent and adsorption time to confirm the tendency for reactivity between prepared adsorbents and Pb^{2+} ions and establish the best adsorption conditions (see Supplementary Figs. 7 and 8). Consequently, we determined the experimental conditions for further Pb removal/separation, and the best effect for Pb removal/adsorption was confirmed on DMF (among DMF, dimethyl sulfoxide (DMSO) and *N*-Methyl-2-pyrrolidone (NMP)), 70 mg of HAP/Fe, and after 30 min. Furthermore, HAP and HAP/Fe show excellent adsorption properties in aqueous solution (water) and non-aqueous aprotic polar-based solution (DMF, in this study), despite the Pb-adsorption mechanism being changed from ion exchange to electrostatic interaction (see Supplementary Fig. 9 for details on adsorption kinetics and absorption mechanisms). This means that the DMF molecule does not affect the adsorption of Pb ion at the adsorbent's surface. This is supported by reaction modelling between the adsorbent and Pb at the surface of adsorbents (HAP or HAP/Fe) with DMF condition. In our density functional theory (DFT) calculations, DMF molecules preferentially interact with calcium (Ca) atoms on the HAP surface via oxygen atoms, whereas metal atoms (Pb and Fe) form bonds with oxygen atoms on the surface. Different adsorption mechanisms of DMF and metal atoms are consistent with the excellent adsorption of Pb in both water and DMF solutions in experiments.

Table 1 | Surface properties of the HAP, HAP/IONPs and HAP/Fe

	BET surface area ($m^2 g^{-1}$)	BJH total pore volume ($cm^3 g^{-1}$)	Average pore size[a] (nm)	Zeta potential[b] (mV)
HAP	127.4	0.424	12.3	−22.5
HAP/IONPs	42.4	0.125	27.0	−17.5
HAP/Fe	152.9	0.514	17.1	−27.6

[a]Average pore size distribution according to the BJH method. [b]Measured zeta potential of particles dispersed in DMF solution.

Origin of improved Pb adsorption properties of HAP/Fe

The surface charge of absorbents plays an important role in Pb^{2+} ion absorption. In particular, absorbents with a negative surface charge show higher interaction with Pb^{2+} ions. Thus, to understand the impact of Fe on the surface charge of HAPs, we analysed the electrochemical properties of HAP/Fe using X-ray photoelectron spectroscopy (XPS) and zeta potentials. XPS spectra in Fig. 2a display the Fe 2*p* peaks for HAP/Fe, HAP/IONPs and HAP. After reduction annealing at 500 °C, HAP/Fe exhibits a distinct Fe(0) peak at 706 eV, which is well matched with the XRD results of transformed Fe in HAP/Fe. We also confirmed that the transformed Fe in HAP/Fe has many peaks between 710 and ~730 eV, corresponding to Fe^{2+} and Fe^{3+}. Furthermore, the oxygen 1*s* peak of HAP/Fe has been shifted toward higher bonding energies in the XPS spectra of oxygen 1*s* of HAP/Fe (see the upper panel in Supplementary Fig. 10). In addition, as shown in Supplementary Fig. 11, the shift of the (002) plane of the HAP peak to a higher angle was observed for the HAP/Fe samples whereas there was no change for XRD peaks of pure HAP, reduction-annealed HAP without IONPs (HAP_RA) and HAP/IONPs. This means that the lattice constant of HAP was decreased due to the doping of Fe^{2+} or Fe^{3+}, which had smaller ionic radii than

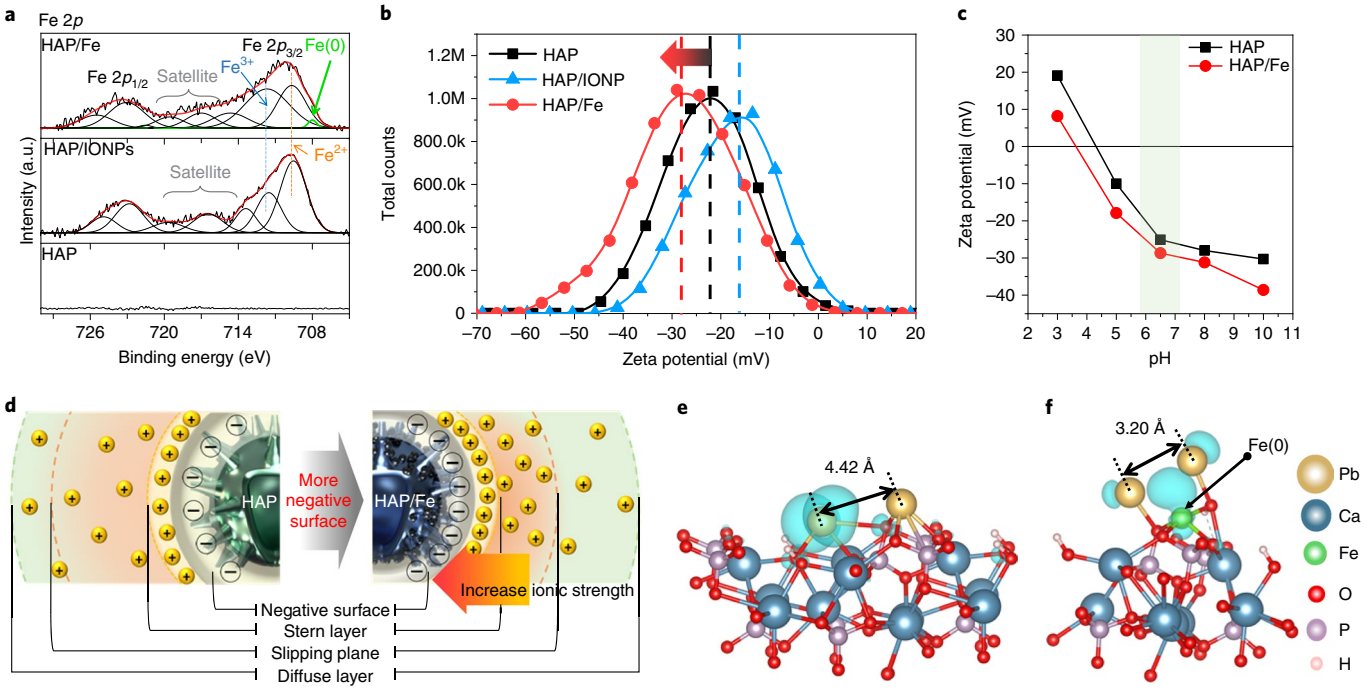

Fig. 2 | Impact of Fe incorporating on surface properties of HAP. a, XPS spectra of Fe 2*p* peaks of HAP/Fe, HAP/IONPs and HAP. The peak at 706 eV in HAP/Fe indicates the formation of Fe metal (Fe(0)). Binding energy was calibrated to carbon (C) 1s peak. **b**, Zeta potentials of HAP, HAP/IONPs and HAP/Fe in DMF. **c**, pH dependence of zeta potentials for HAP/Fe and HAP. We conducted a Pb-absorption experiment in the range of the green section. **d**, Schematic diagram of surface-charge difference between HAP and HAP/Fe for charge-attraction ability. **e**,**f**, Schematic illustration of the crystal structure of HAP (**e**) and HAP/Fe (**f**) determined by DFT calculation of Pb adsorption, which demonstrates a Pb–Fe–Pb interaction that can increase the surface density of Pb.

the Ca^{2+} at the HAP surface[26]. Even though the phase of Fe nanoparticles on HAP/Fe mainly remains as Fe metals, the Fe^{2+}/Fe^{3+} ions on the HAP surface have bonded with the neighbouring oxygen in a form of Ca–O–Fe as doping[26].

The zeta potential measurement was used to explore the surface charge of samples in Fig. 2b. The zeta potentials of HAP, HAP/IONPs and HAP/Fe are −22.28, −16.17 and −27.98 mV, respectively. Typically, HAP has a negatively charged oxygen surface from phosphate, which leads to a negative surface charge in neutral pH[22]. Because the isoelectric point of IONPs is higher than 8, the zeta potential of HAP/IONPs is more strongly positive than that of HAPs[27]. Unlike HAP/IONPs, the incorporated Fe alters the surface potential due to its imbalanced charge distribution, leading to a stronger negative potential shift than that of pristine HAP[28,29]. As shown in Fig. 2c, the zeta potential value of HAP/Fe is lower than that of HAP in the entire pH range from 3 to 10. On the basis of the results of electrostatic surface properties of synthetic particles, the difference in ability of cation attraction between HAP and HAP/Fe is expressed in Fig. 2d. The schematic diagrams in Fig. 2d represent the change in the electrical double layer, with a more compact Stern layer (the first layer of the electrical double layer) of cations strongly bound to a negatively charged surface layer after Fe decoration on the HAP surface. A more strongly negatively charged HAP/Fe particle enhances the electrostatic interaction with a positively charged Pb^{2+} cation. That is, bonded Fe on the surface of HAPs would enable an increase in the adsorption density of Pb^{2+} ions with higher ionic strength. Consequently, a higher density of Pb^{2+} ions surrounding the surface leads to the formation of a narrower slipping plane, in which the electrostatic force is drastically reduced. This means that a higher concentration of positively charged Pb^{2+} ions would be adsorbed with a small screening length on a strongly negatively charged HAP/Fe surface.

To confirm our experimental hypothesis about Fe effects on the surface charge of HAP, we explored surface modelling of HAP and HAP/Fe with Pb via first-principles DFT simulations. Before simulating Pb adsorption with HAP and HAP/Fe, we calculated the preferential adsorption site of Pb. As shown in Supplementary Fig. 12 and Supplementary Table 2, Pb shows a strong preference for three Pb–O bonds, and this is well matched to the XPS results (Supplementary Fig. 9c). When an additional Pb atom is incorporated near an adsorbed Pb atom, the second Pb atom also forms two or three Pb–O bonds. The stabilized distance between these neighbouring Pb atoms is 4.4 Å. We find an effect on the absorption in Fe-incorporated HAP, owing to a chemical interaction between Pb and Fe. In the presence of Fe, the stabilized distance between these Pb atoms is 3.2 Å, as shown in Fig. 2e,f. A higher density of Pb atoms could be adsorbed on the HAP/Fe surface because of the closely packed Pb atoms, which can explain the enhanced Pb-removal property of the HAP/Fe composite. However, if Fe atoms cover a large portion of the HAP surface, the absorbance of Pb should be impeded because Fe–O bonds are stronger than Pb–O bonds.

Fe decoration effects on HAP for Pb capturability

We validated the correlation between the enhanced surface property and reduced adsorption active site after Fe decorating through examining the Pb-adsorption property of HAP/Fe with different Fe concentrations. Figure 3a presents the Pb concentration after filtration using HAP/Fe with different Fe amounts from 0 to 15 wt%. The Pb removal of HAP/Fe increased as the amount of Fe loading increased, until 10 wt%. Even the Fe has a negligible Pb-adsorption property. Above 10 wt% of Fe loading, the amount of adsorbed Pb decreases. This tendency supports the results of theoretical modelling of the Fe effect. Figure 3b illustrates how Pb atoms would be distributed when adsorbed onto a HAP or HAP/Fe surface. In our

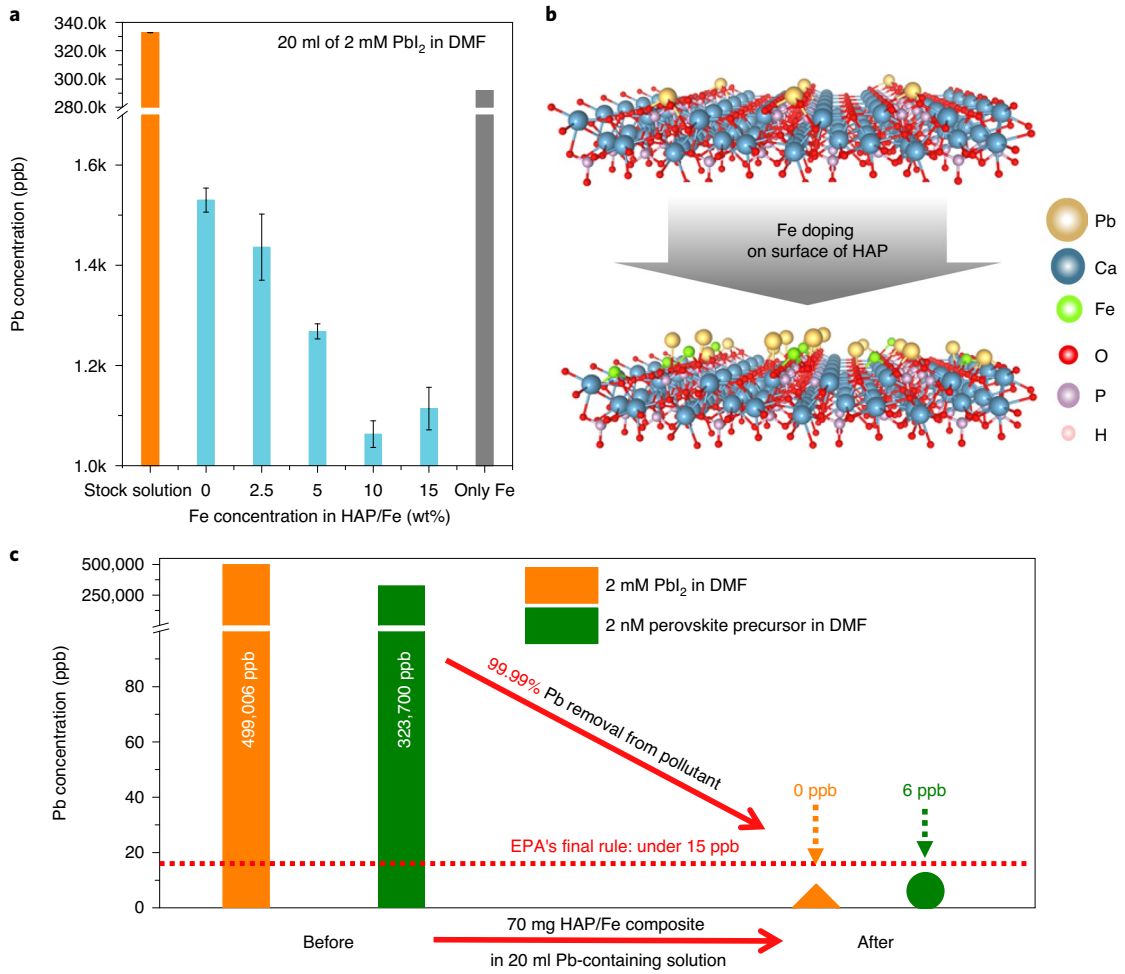

Fig. 3 | Fe effects on HAP for Pb capturability. a, Concentration of Pb before and after Pb adsorption using a HAP/Fe composite with different weight percentage Fe in the HAP/Fe; 20 ml of 2 mM of the PbI_2/DMF solution are used as a Pb stock solution. Error bars represent the mean ± s.d. **b**, DFT simulation of Pb adsorption on the surface of HAP and HAP/Fe, which demonstrates that the number of bounded Pb ions is increased with Fe doping on the surface of HAP. **c**, Removal of the Pb element in PbI_2/DMF and typical perovskite precursor composed of PbI_2, methylammonium iodide and DMF using HAP/Fe.

DFT calculations, we consistently found that a single Pb atom forms three Pb–O bonds. An additional Pb atom can be adsorbed in the vicinity of the pre-adsorbed Pb atom, but it is not thermodynamically favoured, indicating that Pb atoms will be adsorbed uniformly on the HAP surface. A single Fe atom, however, was found to form four Fe–O bonds on the HAP surface. When we located an additional Pb atom near the adsorbed Fe atom, the Pb atom can make various configurations with one, two or three Pb–O bond(s). Such structural diversity enables adsorption of two Pb atoms near an Fe atom with a short distance between them, as shown in Fig. 2f, resulting in higher adsorption of Pb atoms on the HAP/Fe surface than on the bare HAP surface.

Figure 3c shows the Pb-adsorption properties of HAP/Fe in PbI_2–DMF and perovskite precursor solution, which is a representative case of Pb-containing non-aqueous solution waste. To determine the case-experimental condition, we investigated Pb adsorption using various conditions, such as Pb concentration and amount of adsorbent (see Supplementary Fig. 7), and the most effective condition for Pb removal/adsorption was confirmed on DMF (among DMF, DMSO and NMP), 70 mg of HAP/Fe, and after 30 min. After a 30-min reaction between 70 mg of each adsorbent (PbI_2–DMF and perovskite precursor solution under continuous shaking), the residual Pb concentration falls to below 15 ppb in both solutions, which means it is a safe solvent according to the EPA rule[30,31]. Supplementary Video 1 shows the typical protocol for Pb removal/separation, including Pb adsorption and Pb separation from a solvent using HAP/Fe composite. Further, Pb adsorption by HAP/Fe in non-aqueous solvents has enormous potential to be extended to the removal of other toxic heavy metals, such as Sn^{2+}, which is widely used in narrow-bandgap perovskite materials[32]. Thus, we applied the HAP/Fe adsorbent for Sn^{2+} removal (20 ml of 2 mM SnI_2 in DMF), and HAP/Fe shows an excellent absorbing property, as shown in Supplementary Fig. 13.

Demonstration of the Pb management system

Figure 4 shows our demonstrated Pb management system and covers the complete steps related to PCSs. We already reported on the recycling process of the substrate from degraded devices, as illustrated in step 1 and step 2 in Fig. 4a, using the selective dissolving approach[8]. Step 3 in Fig. 4a shows our proposed Pb purifying and recycling process using HAP/Fe composite. To use the magnetic properties of HAP/Fe in real Pb-containing pollutants, an electromagnetic coil-wrapped purifying system is devised, as shown in Supplementary Fig. 14. The pseudo-Pb-pollutants were prepared by dissolving 20 pieces of real perovskite solar modules with a 16 cm^2 area in 20 ml of DMF containing metal electrodes, hole-transport

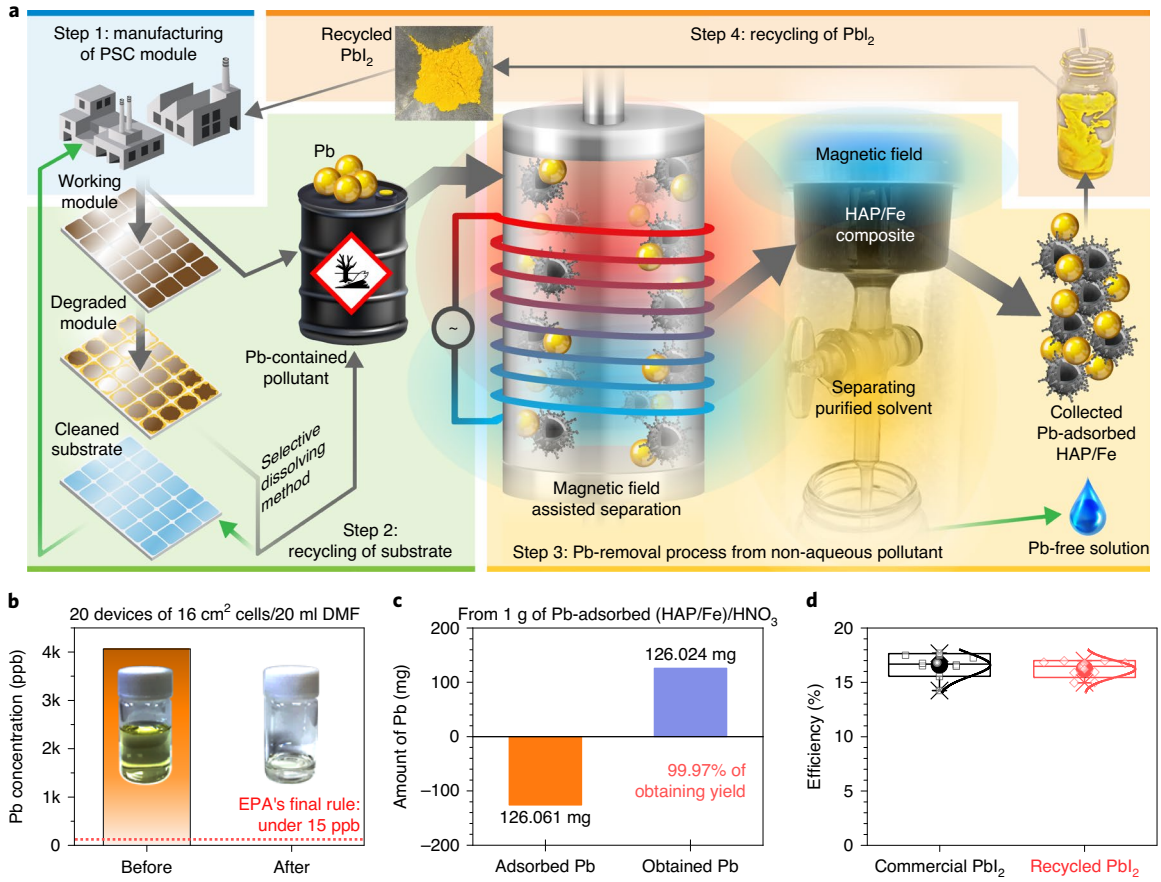

Fig. 4 | Illustration of the use of HAP/Fe composite for treating a Pb-containing solution pollutant and PbI_2 regaining process after Pb removal/separation. a, Process of Pb removal/separation from Pb-containing pollutant formed during manufacturing and recycling of PSCs. The grey arrow represents a Pb-containing process, and the green arrow represents a Pb-free process. Step 1: manufacturing PSC modules. Step 2: substrate recycling process from degraded PSC modules via selective dissolving method. Step 3: Pb-removal process from perovskite industrial pollutant using a HAP/Fe composite and electromagnetic separating system. A photograph of the actual electromagnetic separating system is shown in Supplementary Fig. 14. Step 4: recycling of Pb by forming PbI_2 from Pb-adsorbed HAP/Fe composite. **b**, Pb concentration after Pb removal/separation using a HAP/Fe composite and electromagnetic separating system. Twenty modules with a 16 cm^2 device area were recycled in 20 ml DMF. **c**, The adsorbed and recycled Pb amount from 1 g Pb-adsorbed HAP/Fe. The detailed recycling process from Pb-adsorbed HAP/Fe is described in the experimental section. **d**, Statistics of efficiencies of perovskite solar cells using commercial PbI_2 (control device, black) and recycled PbI_2 from a Pb-adsorbed HAP/Fe composite.

molecules and numerous elements from perovskite compositions. The HAP/Fe composite and pseudo-Pb-pollutant are placed together into an electromagnetic coil-wrapped bottle and are then shaken to adsorb the Pb. After completing the Pb adsorption, we applied an electromagnetic field across the bottle, and Pb-adsorbed HAP/Fe composites were attached to the wall of the container. Pb-separated solvents flowed out from this bottle and a purified solvent that meets EPA regulations on Pb emissions (below 15 ppb), from 4,000 ppb in the initial pseudo-Pb-pollutant, as shown in Fig. 4b (ref. [30]). Furthermore, to realize a zero Pb-pollutant policy in the PSC market, we tested the feasibility of recycling Pb from collected Pb-adsorbed HAP/Fe composites by reprecipitating the PbI_2, which is an essential raw material for perovskite. In general, HAP particles can be dissolved in an H_2O-based solution with pH values less than 2 (ref. [22]); by contrast, PbI_2 has low solubility in H_2O regardless of the pH. To use these differences of solubilities, we dispersed Pb-adsorbed HAP/Fe into 20 ml of 0.5 M HNO_3 acidic solution. Then, 1 M of KI solution was poured into the solution to recrystallize PbI_2, as shown in step 4 in Fig. 4a. Consequently, we have reached the 99.97% of Pb recycling yield (Fig. 4c). The obtained PbI_2 powder is confirmed using the photo images in step 4 of Fig. 4a and XRD patterns of obtained PbI_2 in Supplementary Fig. 15, respectively. Figure 4d and Supplementary Table 3 informed the quality of collected PbI_2 as a perovskite raw material with similar device performance as commercially available PbI_2. The performance of the device has a strong correlation with the quality of the raw material. Therefore, recycled PbI_2 is comparable in quality to commercial PbI_2; thus, our study enables a zero-lead-emission route for future perovskite technologies.

Conclusions

In summary, we successfully synthesized a new Pb adsorbent, a HAP/Fe composite with enhanced Pb uptake capacity and magnetism, by incorporating Fe. The prepared HAP/Fe composites demonstrate a reinforced Pb-adsorption property that meets EPA regulations on Pb emissions (below 15 ppb) and an expedient and easy collection of Pb-adsorbed HAP/Fe composites from a purified DMF. Our experimental and theoretical investigations cross-verified that the embodied Fe induced a shift to a stronger negative charge and improved the electrostatic interaction at the surface of HAP by charge delocalization, consequently enhancing the Pb-adsorption property. Furthermore, the reinforced Pb adsorption of HAP/Fe has led to the demonstration of a complete Pb management system (including removal and recycling of Pb^{2+}

ions) during the entire PSC fabrication process with a 99.97% Pb recycling yield. Our approach paves a way for PSC manufacturing with zero Pb emission and, by extension, provides the methodology for recycling and managing lead from waste devices to allay concerns on Pb-related environmental issues. Moreover, this study demonstrates the potentials of using the economical and bio- and environment-friendly adsorbents for heavy metal management in pollutants, including the organic solvents that have been used conventionally in the industry.

Methods

Materials. Poly(sodium 4-styrene sulfonate) (PSS, 30 wt.% solution in water, Sigma-Aldrich, MW 70,000), calcium nitrate tetrahydrate ($Ca(NO_3)_2{\cdot}4H_2O$, 99%, Sigma-Aldrich), sodium carbonate (Na_2CO_3, 99%, Sigma-Aldrich), disodium hydrogen phosphate (Na_2HPO_4, 99%, Sigma-Aldrich), (3-aminopropyl) triethoxysilane (APTES, $H_2N(CH_2)_3Si(OC_2H_5)_3$), citric acid ($C_6H_8O_7$, 99%, Sigma-Aldrich), *N*,*N*-dimethylformamide (DMF, Sigma-Aldrich), dimethyl sulfoxide (DMSO, Sigma-Aldrich), lead nitrate ($Pb(NO_3)_2$, 99%, Sigma-Aldrich), and lead iodide (PbI_2, 99%, Sigma-Aldrich) were used as received, without further purification.

Synthesis of hollow HAP spheres. Hollow HAP spheres (HAPs) were synthesized using the Kirkendall effect assisted ion-exchange method with a $CaCO_3$ template prepared using a fast precipitation method[24,25]. Typically, for $CaCO_3$ spheres, 15 mmol $Ca(NO_3)_2$ and Na_2CO_3 are dissolved in 600 ml of PSS with a concentration of 25 g l^{-1} and 120 ml deionized water, respectively. Then, the Na_2CO_3 solution is added to $Ca(NO_3)_2$ and PSS mixed solution with constant stirring for 30 min. After collecting the white precipitations via centrifugation, the powder is washed several times with deionized water. To convert the $CaCO_3$ spheres into HAPs, 500 ml of 0.5 M Na_2HPO_4 were added into the obtained $CaCO_3$ spheres dispersed in 500 ml of water. The pH of the mixture was adjusted to 11.0 using ammonia solution, and it was poured into a glass bottle, sealed and maintained at 120 °C for 4 h. Afterwards, the resultant powder was collected via centrifugation and washed several times with deionized water and ethanol, then dried at 60 °C for 2 h in a vacuum oven.

Fe nanoparticles surface-decorating on HAPs for magnetic-property functionalizing. To give magnetic properties to HAPs, IONPs were attached to the surface of HAPs. Surface functionalization was conducted on the HAPs and IONPs. For the amino-functionalized HAPs, 100 mg of HAPs was put into 100 ml of APTES solution. After that, the HAPs-dispersed APTES solution was heated at 70 °C under vigorous stirring for 3 h to amino-functionalize the HAP surface. The resulting composites were washed several times with ethanol via centrifugation. For carboxy-functionalized IONPs (COOH-IONPs), a dispersion of 10 mg of the IONPs in 1 ml of chloroform was added to 10 ml of citric acid/DMSO solution with a concentration of 20 mg ml^{-1}, and the mixture was heated at 70 °C for 3 h with vigorous stirring. After washing the COOH-IONPs using ethanol, the nanoparticles were dispersed in ethanol with a concentration of 10 mg ml^{-1}. Afterwards, we mixed the COOH-IONPs and amino-functionalized HAP with different weight ratio for 3 h at room temperature. In general, to attach the COOH-IONPs on amino-functionalized HAP, 1 g of amino-terminated HAP powder was added to 10 ml of COOH-IONPs solution (10 mg ml^{-1}). The resultant magnetic composites were separated using a permanent Nd magnet. The prepared HAP/IONPs composites were annealed at 500 °C under a reductive atmosphere with 5 v/v% of H_2/N_2 mixed gas to take away the functionalized polymer ligand and form HAP/Fe composites.

Materials characterization. The morphology and size of the particles were characterized using an FE-SEM (JSM-7600F, JEOL) and an HR-TEM (JEM-3010, JEOL). Crystallographic characterization was conducted using XRD (Bruker advanced D8, $\lambda = 1.5406$ Å). The surface area and pore size distribution of samples were determined using BET and BJH analysis (SA3100, Berckman Coulter). The binding energies of the elements for the surface of the samples were measured using X-ray photoelectron spectroscopy (ESCA 2000, VG Microtech). The surface charge of the samples was estimated using a zeta-potential assay. The zeta potentials of samples were characterized using a zetasizer Nano Z90 potential analyser (Malvern). Magnetic measurements for magnetization versus magnetic field (M–H) curves were analysed using a vibrating sample magnetometer (MPMS3-Evercool, Quantum Design). The M–H loops were carried out in a field sweep from −50,000 to +50,000 Oe at 300 K.

Investigation of Pb adsorbability. Investigation of Pb-ion adsorbability was performed at room temperature by shaking a series of bottles at predetermined times using a shaker (SHR-1D, Wiseshake) at 120 r.p.m. Each bottle contained the desired quantity of the composites in a predetermined concentration of lead ion solution. $Pb(NO_3)_2$ and PbI_2 were used for the water and aprotic polar solvent (that is, DMF) batch adsorption experiments, respectively. After the Pb-ion adsorption process, HAP samples were separated by centrifuging at 8,000 r.p.m. for 10 min, and the HAP/IONPs and HAP/Fe samples were separated using a permanent Nd magnet. The residual Pb concentration in the solution was measured through inductively coupled plasma–mass spectrometry (Agilent 7500). The percentage removal of Pb ion from the solution was determined using the following equation:

$$\text{Removal\%} = \frac{C_0 - C_f}{C_0} \times 100$$

where C_0 is the initial concentration of a Pb ion, and C_f is the final concentration of the Pb ion.

Materials modelling. To provide an understanding of the adsorption at the atomistic level, we performed first-principles DFT calculations and investigated the adsorption properties of Pb and Fe ions on the [010] HAP surface. We used the generalized gradient approximation parameterized by Perdew, Burke and Ernzerhof[33] and the projector-augmented wave method[34], implemented in the Vienna ab initio simulation package code[35]. For a better description of the dispersion interaction, the DFT-D2 method proposed by Grimme was used[36]. A higher-energy cutoff of 500 eV was used to optimize the bulk lattice constants. The optimized lattice constants were 9.49 Å and 6.84 Å, comparable to the experimental values of 9.42 Å and 6.89 Å[37]. For the slab calculations, an energy cutoff of 400 eV was used throughout the calculations. Spin-polarized calculations were done to account for spins of the Fe ions. The thickness of the vacuum and slab were about 14 and 11 Å, respectively. While atoms at one surface were fully relaxed, atoms at the other surface were frozen to remove interaction between the surfaces. Considering the strong P–O bonds, we broke only Ca–O bonds to generate a surface model. A flat plateau of the electrostatic potential in the vacuum region was obtained, indicating the absence of a long-range electric dipole.

Pb removal/separation pilot equipment. To address the use possibility of HAP/Fe for a continuous magnetic separation system, we fabricated Pb-removal pilot equipment, including electromagnetic coils, a magnetic controller and a glass bottle with a stopcock. First, 250 mg of HAP/Fe powder was added to 70 ml of 2 mM PbI_2/DMF solution. The Pb adsorption was performed using pilot equipment, switching the electromagnetic field on and off several times to give a chance for a reaction between the HAP/Fe and Pb ions, instead of shaking the mixture bottle. After the reaction, the HAP/Fe particles were attracted by the generated electromagnetic field, and the Pb-free solution was dispensed from the burette.

Recycling of PbI_2 from the Pb-adsorbed HAP/Fe. The 1 g of Pb-adsorbed HAP/Fe was dissolved in 20 ml of pH 2 solution. In this study, we prepared a 0.5 M HNO_3 solution with pH 2. The HAP/Fe composite was quickly dissolved in this solution within a few minutes. Afterwards, a KI (1 M) solution was added to the Pb-ions-included solution until no more of the yellow product was formed. The yellow PbI_2 precipitate was washed with water and methanol and collected by centrifugation. The regained PbI_2 was dried in a vacuum oven at 60 °C for 3 h. Then, the dried PbI_2 powder was stored in a glovebox with an N_2 atmosphere. The recycling yield of Pb ion from adsorbed Pb on HAP/Fe composites was determined using the following equation:

$$\text{Pb recycling yield (\%)} = \frac{X_0 - X_f}{X_0} \times 100$$

where X_0 is the concentration of Pb ions in a Pb dissolved solution, and X_f is a concentration of the Pb ion after recycling.

Fabrication and characterization of perovskite solar cells using recycled PbI_2. Laser-scribed FTO-coated glass substrates were cleaned with deionized water, ethanol and acetone. A compact TiO_2 was coated on the prepared substrates by spin-coating at 4,000 r.p.m. for 30 s, using 0.1 M titanium diisopropoxide bis(acetylacetonate) solution (75% in 2-propanol, Sigma-Aldrich) in 1-butanol, and then baking for 5 min at 135 °C. They were then annealed at 500 °C for 60 min. Subsequently, a 0.04 M $TiCl_4$ water solution was used to treat the TiO_2 compact layer surface at 70 °C for 20 min, followed by another heat treatment at 150 °C for 30 min. For the perovskite layer, the 1.5 mmol of recycled PbI_2 was dissolved in a 1 ml mixture solution of DMF and DMSO (8:2 volume ratio) at 70 °C for 30 min. The PbI_2 precursor was spin-coated on the prepared substrate at 2,500 r.p.m. for 30 s, and then a cation halide solution mixture (0.08 g formamidinium iodide, 0.008 g methylammonium bromide and 0.008 g methylammonium chloride in 1 ml 2-propanol) was dropped on the PbI_2 films, followed by quick spin-coating at 5,000 r.p.m. for 30 s. Then, the semi-transparent brown colour films were heated on a hotplate at 150 °C for 20 min. For the control device, we used high-purity PbI_2 powder (TCI chemicals, 99.99%, trace-metal basis for perovskite precursor), and a perovskite film was fabricated using the same method. After cooling to room temperature, hole-transport material was deposited by spin-coating at 4,000 r.p.m. for 30 s. The hole-transport material solution consists of 36 mg (2,29,7,79tetrakis (N,N-di-p-methoxyphenylamine)-9,9-spirobifluorene)-(spiro-OMeTAD), 14.4 µl 4-tert-butylpyridine, and 8.8 µl of 520 mg m l^{-1} lithium bis(trifluoromethylsulfonyl) imide acetonitrile solution dissolved in 0.5 ml chlorobenzene. The photovoltaic

properties were measured using a solar simulator (Newport Oriel Solar 3A Class AAA, 64023A) equipped with a 450-W xenon lamp (Newport 6279NS), which was calibrated using a standard silicon photovoltaic cell (Rc-1000-TC-KG5-N, VLSI Standards) and a potentiostat (CHI 600D, CH Instruments). All devices were measured by masking the active area with a 0.14-cm^2 mask. Current density-voltage (J-V) characteristics for all devices were measured at a voltage scan rate of 0.1 Vs^{-1}.

Reporting Summary. Further information on research design is available in the Nature Research Reporting Summary linked to this article.

Data availability

The data that support the findings of this study are available within the Article and its Supplementary Information file and from the corresponding author upon reasonable request. Any available information on data resources used in or produced for the paper is provided.

Received: 15 October 2019; Accepted: 28 June 2020;
Published online: 03 August 2020

References

1. Jeon, N. J. et al. A fluorene-terminated hole-transporting material for highly efficient and stable perovskite solar cells. *Nat. Energy* **3**, 682–689 (2018).
2. Yang, W. S. et al. Iodide management in formamidinium-lead-halide-based perovskite layers for efficient solar cells. *Science* **356**, 1376–1379 (2017).
3. Christians, J. A. et al. Tailored interfaces of unencapsulated perovskite solar cells for >1,000 hour operational stability. *Nat. Energy* **3**, 68–74 (2018).
4. Deng, Y. H. et al. Surfactant-controlled ink drying enables high-speed deposition of perovskite films for efficient photovoltaic modules. *Nat. Energy* **3**, 560–566 (2018).
5. Yang, M. J. et al. Highly efficient perovskite solar modules by scalable fabrication and interconnection optimization. *ACS Energy Lett.* **3**, 322–328 (2018).
6. Kim, D. H., Whitaker, J. B., Li, Z., van Hest, M. F. A. M. & Zhu, K. Outlook and challenges of perovskite solar cells toward terawatt-scale photovoltaic module technology. *Joule* **2**, 1437–1451 (2018).
7. Babayigit, A., Ethirajan, A., Muller, M. & Conings, B. Toxicity of organometal halide perovskite solar cells. *Nat. Mater.* **15**, 247–251 (2016).
8. Kim, B. J. et al. Selective dissolution of halide perovskites as a step towards recycling solar cells. *Nat. Commun.* **7**, 11735 (2016).
9. Park, N.-G., Grätzel, M., Miyasaka, T., Zhu, K. & Emery, K. Towards stable and commercially available perovskite solar cells. *Nat. Energy* **1**, 16152 (2016).
10. Abate, A. Perovskite solar cells go lead free. *Joule* **1**, 659–664 (2017).
11. Lin-Fu, J. S. Vulnerability of children to lead exposure and toxicity (second of two parts). *N. Engl. J. Med.* **289**, 1289–1293 (1973).
12. Matlock, M. M., Howerton, B. S. & Atwood, D. A. Chemical precipitation of lead from lead battery recycling plant wastewater. *Ind. Eng. Chem. Res.* **41**, 1579–1582 (2002).
13. Bolisetty, S. & Mezzenga, R. Amyloid-carbon hybrid membranes for universal water purification. *Nat. Nanotechnol.* **11**, 365–371 (2016).
14. Dabrowski, A., Hubicki, Z., Podkościelny, P. & Robens, E. Selective removal of the heavy metal ions from waters and industrial wastewaters by ion-exchange method. *Chemosphere* **56**, 91–106 (2004).
15. Ali, I. & Gupta, V. K. Advances in water treatment by adsorption technology. *Nat. Protoc.* **1**, 2661–2667 (2006).
16. Zhao, J. et al. Facile preparation of a self-assembled Artemia cyst shell–TiO_2–MoS_2 porous composite structure with highly efficient catalytic reduction of nitro compounds for wastewater treatment. *Nanotechnology* **31**, 085603 (2020).
17. Yuan, Q. L. et al. Facet-dependent selective adsorption of Mn-doped alpha-Fe_2O_3 nanocrystals toward heavy-metal ions. *Chem. Mater.* **29**, 10198–10205 (2017).
18. Huang, X. et al. Facile preparation of hierarchical AgNP-loaded MXene/Fe_3O_4/polymer nanocomposites by electrospinning with enhanced catalytic performance for wastewater treatment. *ACS Omega* **4**, 1897–1906 (2019).
19. Wang, C. et al. Facile preparation and catalytic performance characterization of AuNPs-loaded hierarchical electrospun composite fibers by solvent vapor annealing treatment. *Colloids Surf. A* **61**, 283–291 (2019).
20. Bailliez, S., Nzihou, A., Bèche, E. & Flamant, G. Removal of lead (Pb) by hydroxyapatite sorbent. *Process Saf. Environ. Prot.* **82**, 175–180 (2004).
21. Meski, S., Ziani, S. & Khireddine, H. Removal of lead ions by hydroxyapatite prepared from the egg shell. *J. Chem. Eng. Data* **55**, 3923–3928 (2010).
22. Elliott, J. C. *Structure and Chemistry of the Apatites and Other Calcium Orthophosphates* (Elsevier, 1994).
23. Ignjatović, N. L. et al. Rare-earth (Gd^{3+},Yb^{3+}/Tm^{3+}, Eu^{3+}) co-doped hydroxyapatite as magnetic, up-conversion and down-conversion materials for multimodal imaging. *Sci. Rep.* **9**, 16305 (2019).
24. Lai, W. et al. Hydrothermal fabrication of porous hollow hydroxyapatite microspheres for a drug delivery system. *Mat. Sci. Eng. C.* **62**, 166–172 (2016).
25. Wang, Y. S., Moo, Y. X., Chen, C., Gunawan, P. & Xu, R. Fast precipitation of uniform $CaCO_3$ nanospheres and their transformation to hollow hydroxyapatite nanospheres. *J. Colloid Interface Sci.* **352**, 393–400 (2010).
26. Park, S. Y. et al. Osteoinductive superparamagnetic Fe nanocrystal/calcium phosphate heterostructured microspheres. *Nanoscale* **9**, 19145–19153 (2017).
27. Singh., N. et al. Polydopamine modified superparamagnetic iron oxide nanoparticles as multifunctional nanocarrier for targeted prostate cancer treatment. *Nanomaterials* **9**, 138 (2019).
28. Iannotti, V. et al. Fe-doping-induced magnetism in nano-hydroxyapatites. *Inorg. Chem.* **56**, 4446–44583 (2017).
29. Kawabata, S. et al. *Synthesis and Characterization of Wet Chemically Derived Magnetite-HAP Hybrid Nanoparticles* (American Ceramic Society, 2010).
30. Hailegnaw, B., Kirmayer, S., Edri, E., Hodes, G. & Cahen, D. Rain on methylammonium lead iodide based perovskites: possible environmental effects of perovskite solar cells. *J. Phys. Chem. Lett.* **6**, 1543–1547 (2015).
31. *Lead Laws and Regulations* (EPA, 2015).
32. Babayigit, A. et al. Assessing the toxicity of Pb- and Sn-based perovskite solar cells in model organism *Danio rerio*. *Sci. Rep.* **6**, 18721 (2016).
33. Perdew, J. P., Burke, K. & Ernzerhof, M. Generalized gradient approximation made simple. *Phys. Rev. Lett.* **77**, 3865–3868 (1996).
34. Blöchl, P. E. Projector augmented-wave method. *Phys. Rev. B* **50**, 17953–17979 (1994).
35. Kresse, G. & Furthmüller, J. Efficient iterative schemes for ab initio total-energy calculations using a plane-wave basis set. *Phys. Rev. B* **54**, 11169–11186 (1996).
36. Grimme, S. Semiempirical GGA-type density functional constructed with a long-range dispersion correction. *J. Comput. Chem.* **27**, 1787–1799 (2006).
37. Markovic, M., Flowler, B. O. & Tung, M. S. Preparation and comprehensive characterization of a calcium hydroxyapatite reference material. *J. Res. Natl Inst. Stand. Technol.* **109**, 553–568 (2004).

Acknowledgements

This work was supported by the Global Frontier R&D Program on Center for Multiscale Energy System funded by the National Research Foundation (under contract no. 2012M3A6A7054855), the Alchemist project of the Korea Institute of Energy Technology Evaluation and Planning (KETEP) granted financial resource from the Ministry of Trade, Industry & Energy (20193091010310), and the National Research Foundation of Korea (NRF) grant funded by the Korea government (MSIP) (NRF-2018M3C1B7021994 and 2019R1F1A1064095). This research was partially supported by the Ministry of Science, ICT and the Future Planning as Global Frontier Project (CAMM-2019M3A6B3030638). This research was also supported by the Defense Challengeable Future Technology Program of the Agency for Defense Development, Republic of Korea. The work at the National Renewable Energy Laboratory (NREL) was supported by the De-Risking Halide Perovskite Solar Cells programme of the National Center for Photovoltaics, funded by the Office of Energy Efficiency and Renewable Energy, Solar Energy Technologies Office, US Department of Energy (DOE) under contract no. DE-AC36-08GO28308 with the Alliance for Sustainable Energy, a Limited Liability Company (LLC), and the Manager and Operator of NREL. The views expressed in the article do not necessarily represent the views of the DOE or the US Government. Via our membership of the UK's HEC Materials Chemistry Consortium, which is funded by EPSRC (EP/L000202), this work used the ARCHER UK National Supercomputing Service (http://www.archer.ac.uk).

Author contributions

H.S.J. and D.H.K. supervised this work. S.Y.P. and D.H.K. conceived the idea and designed the experiments. S.Y.P., D.H.K. and J.-S.P. discussed the mechanism and designed the experiment and theoretical calculations. S.Y.P. carried out the synthesis and characterization of materials and the Pb-management test. S.Y.P. and H.L. conducted the magnetic analysis of materials. J.-S.P. and A.W. designed and performed the theoretical calculations. B.J.K., D.H.K. and K.Z. performed the device fabrication and analysis. S.Y.P., J.-S.P., K.Z., D.H.K. and H.S.J. wrote the first draft of the manuscript, and all authors discussed the results and commented on the manuscript.

Competing interests

The authors declare no competing interests.

Additional information

Supplementary information is available for this paper at https://doi.org/10.1038/s41893-020-0586-6.

Correspondence and requests for materials should be addressed to D.H.K. or H.S.J.

Reprints and permissions information is available at www.nature.com/reprints.

Publisher's note Springer Nature remains neutral with regard to jurisdictional claims in published maps and institutional affiliations.

nature research

Corresponding author(s): Dong Hoe Kim, Hyun Suk Jung

Last updated by author(s): Dec 3, 2019

Reporting Summary

Nature Research wishes to improve the reproducibility of the work that we publish. This form provides structure for consistency and transparency in reporting. For further information on Nature Research policies, see Authors & Referees and the Editorial Policy Checklist.

Statistics

For all statistical analyses, confirm that the following items are present in the figure legend, table legend, main text, or Methods section.

n/a	Confirmed
☐	☒ The exact sample size (*n*) for each experimental group/condition, given as a discrete number and unit of measurement
☐	☒ A statement on whether measurements were taken from distinct samples or whether the same sample was measured repeatedly
☒	☐ The statistical test(s) used AND whether they are one- or two-sided *Only common tests should be described solely by name; describe more complex techniques in the Methods section.*
☒	☐ A description of all covariates tested
☐	☒ A description of any assumptions or corrections, such as tests of normality and adjustment for multiple comparisons
☐	☒ A full description of the statistical parameters including central tendency (e.g. means) or other basic estimates (e.g. regression coefficient) AND variation (e.g. standard deviation) or associated estimates of uncertainty (e.g. confidence intervals)
☒	☐ For null hypothesis testing, the test statistic (e.g. *F*, *t*, *r*) with confidence intervals, effect sizes, degrees of freedom and *P* value noted *Give P values as exact values whenever suitable.*
☒	☐ For Bayesian analysis, information on the choice of priors and Markov chain Monte Carlo settings
☒	☐ For hierarchical and complex designs, identification of the appropriate level for tests and full reporting of outcomes
☒	☐ Estimates of effect sizes (e.g. Cohen's *d*, Pearson's *r*), indicating how they were calculated

Our web collection on statistics for biologists contains articles on many of the points above.

Software and code

Policy information about availability of computer code

Data collection	As it is explained in the Methods of the manuscript, we performed the first-principles density functional theory (DFT) calculations using the Vienna Ab initio Simulation Package (VASP version 5) to obtain the simulation data.
Data analysis	For visualization of atomic structures and the charge densities, we used VESTA (Visualization for Electronic and Structural Analysis) 3, which is an open-source program. No other software was used.

For manuscripts utilizing custom algorithms or software that are central to the research but not yet described in published literature, software must be made available to editors/reviewers. We strongly encourage code deposition in a community repository (e.g. GitHub). See the Nature Research guidelines for submitting code & software for further information.

Data

Policy information about availability of data

All manuscripts must include a data availability statement. This statement should provide the following information, where applicable:

- Accession codes, unique identifiers, or web links for publicly available datasets
- A list of figures that have associated raw data
- A description of any restrictions on data availability

The data that support the findings of this study are available from the corresponding author upon reasonable request.

Field-specific reporting

Please select the one below that is the best fit for your research. If you are not sure, read the appropriate sections before making your selection.

☐ Life sciences ☐ Behavioural & social sciences ☒ Ecological, evolutionary & environmental sciences

For a reference copy of the document with all sections, see nature.com/documents/nr-reporting-summary-flat.pdf

Ecological, evolutionary & environmental sciences study design

All studies must disclose on these points even when the disclosure is negative.

Study description	Lead halide PEROVSKITE is the most standout material in the field of photovoltaics. However, because the treatment of Pb-containing nonaqueous waste during fabrication and continuous exposure to Pb from waste or the device can potentially constitute long-term risks, the environmental, health, and safety (EHS) effects of the materials and processes involved could be a major concern in PSC commercialization. To relieve those concerns, in this research, we introduced Pb management and recycling process using a novel Pb adsorbent with enhanced Pb adsorption property from PEROVSKITE solvents by controlling the surface charge of the host Pb adsorbent. And we also demonstrated successful Pb management to meet the standard of United States Environmental Protection Agency (below a 15 ppb of Pb) and to zero-Pb emission route from fabrication to disposal of PEROVSKITE solar cells. But this research did NOT cover Pb impact study on the biological or environmental field directly.
Research sample	Research samples for Pb ions containing pollutants include that Pb(NO3)2/water, PbI2/aprotic polar solvent, and perovskite pollutant (Twenty modules with a 16 cm2 device area were washed in 20 ml dimethylformamide). And representative Pb-absorbent sample, hydroxyapatite/Fe hollow composites with strong negative charge were prepared by decorating iron oxide nanoparticles on surface of a HAP hollow shell and annealed at 500 ºC for 2 h under a reductive atmosphere. Further details for different condition was explained in the Methods section of the manuscript.
Sampling strategy	Sampling procedures are provided in the Methods section of the manuscript. Briefly, we extracted samples from the Pb containing (or removing) test solution, and the residual lead concentration in the solution was measured through inductively coupled plasma mass spectrometry (ICP-MS).
Data collection	We used data that was collected using standard practice in this type of work, and we have given detailed descriptions as to how this collection is carried out, in Methods of the manuscript.
Timing and spatial scale	The samples were collected at predetermined times, which have given in Methods of the manuscript.
Data exclusions	N/A
Reproducibility	The findings in this paper were remarkably reproducible. Every experiment was performed multiple times (more than 5 times).
Randomization	N/A
Blinding	N/A

Did the study involve field work? ☐ Yes ☒ No

Reporting for specific materials, systems and methods

We require information from authors about some types of materials, experimental systems and methods used in many studies. Here, indicate whether each material, system or method listed is relevant to your study. If you are not sure if a list item applies to your research, read the appropriate section before selecting a response.

Materials & experimental systems

n/a	Involved in the study
☒	☐ Antibodies
☒	☐ Eukaryotic cell lines
☒	☐ Palaeontology
☒	☐ Animals and other organisms
☒	☐ Human research participants
☒	☐ Clinical data

Methods

n/a	Involved in the study
☒	☐ ChIP-seq
☒	☐ Flow cytometry
☒	☐ MRI-based neuroimaging